CRYSTAL GROWTH & DESIGN

Article

Cite This: Cryst. Growth Des. 2018, 18, 5099−5107

pubs.acs.org/crystal

# Epitaxy of Anthraquinone on (100) NaCl: A Quantitative Approach

Willem. J. P. van Enckevort,*[,†] Wim L. Noorduin,[†,§] Sander Graswinckel,[†,∥] Paul Verwer,[‡] and Elias Vlieg[†]

[†]Radboud University, Institute for Molecules and Materials, Heyendaalseweg 135, 6525 ED Nijmegen, The Netherlands

[‡]Akzo Nobel Industrial Chemicals, Salt and Crystallization, Deventer, The Netherlands

Supporting Information

**ABSTRACT:** A growth cell suitable for microscopic in situ observation of well-controlled crystal growth from the vapor phase is used to study the heteroepitaxial growth of anthraquinone crystals on a (100) NaCl substrate. In this, the morphology, orientation, nucleation, and growth rate of the crystals is studied as a function of driving force, $\Delta\mu/kT$. At the lowest $\Delta\mu/kT$, the crystals are block-shaped and show no preferential orientation with respect to the substrate. Increasing the driving force leads to the growth of oriented block- and needle-shaped crystals, which nucleate from macrosteps on the substrate. At the highest $\Delta\mu/kT$, crystals nucleate on the flat surface areas or at monatomic steps on the substrate, resulting in a dramatic increase in epitaxial needle density. Growth rate measurements show an exponential behavior as a function of $\Delta\mu/kT$. In all cases, the supply of growth units proceeds via surface diffusion over the NaCl substrate surface toward the anthraquinone crystals. At the lowest $\Delta\mu/kT$, growth is partly limited by integration of the growth units at the crystal surfaces. At intermediate driving force, kinetic roughening sets in, leading to rounded needle tips. At the highest supersaturation, growth is completely governed by the supply of growth units via surface diffusion, leading to tip splitting as a consequence of morphological instability.

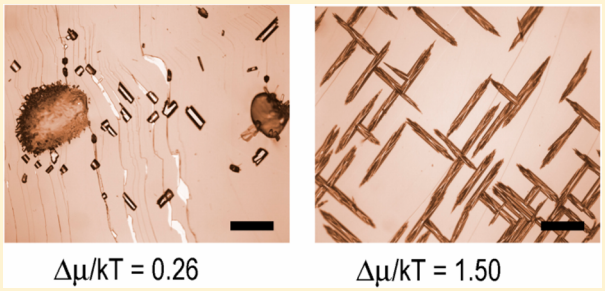




## 1. INTRODUCTION

Heteroepitaxy is the oriented growth of a monocrystalline layer on top of a foreign single crystalline substrate. Basically, this epitaxy can be realized by three different mechanisms.[1−3] If the lattice mismatch between the substrate and grown layer is minimal, then a coherent crystalline film forms by a layer by layer process. This growth mode, known as the Frank−van der Merwe process,[1−3] is the most studied one and finds many applications in the semiconductor industry, e.g., GaInAs on GaAs for LED and laser production.[4] If the lattice mismatch is somewhat larger, first, a few coherent molecular layers are formed, but due to accumulation of stress, their further growth is inhibited. Then, following Stransky−Krastanov, oriented 3D nuclei are formed on top of this layer, which expand and coalesce to a closed layer.[1−3] In a number of cases, the oriented 3D nuclei are directly formed on the substrate without an intermediate layer (Volmer−Weber process[1−3]). Growth of single crystalline layers of GaN via coalescence of 3D nuclei using a buffer layer on top of a sapphire substrate has been well exploited in the production of blue LEDS and lasers.[5−7]

The epitaxial growth of organic crystals on inorganic substrates generally proceeds via the Stranski−Krastanov and the Volmer−Weber mechanisms. Pioneering work on many differerent substrate−guest systems has been performed by Sprangenberg, Neuhaus,[8] Willems,[9] and Sloat and Menzies[10] in the first half of the previous century. In their studies, attention was mainly paid to the geometrical and crystallographic relationships between the 3D guest crystallites and the substrate. After this period, the epitaxy research shifted toward the layer-by-layer growth of inorganic materials for semiconductor applications. With the emergence of organic materials for semiconductor and optoelectronic applications, however, interest in organic epitaxy revived in the last few decades. Two examples are the growth of *para*-sexiphenyl[11] and sexithiophene[12] crystals on KCl (100). Extended reviews on the epitaxial growth of organic compounds on organic and inorganic crystal substrates are given by Simmbrunner et al.[13] and Evans and Spalenka.[14] A major issue today is also the oriented growth of 2D self-assembling molecular monolayers on inorganic substrates.[15−20] This aspect, though, is not considered in our paper, which concentrates on 3D epitaxial nucleation and growth.

Most studies on the 3D epitaxial growth of organic crystals were static and confined to establishing a crystallographic and bonding relationship between the guest and host.[21−28] Less attention was given to the kinetics of nucleation and the mechanism of subsequent growth of the 3D germs on top of the substrate. Neuhaus and several other investigators have shown that anthraquinone deposited on cleaved (100) NaCl surfaces forms well oriented needles with their length direction

Received: April 12, 2018
Revised: July 13, 2018
Published: July 23, 2018

  

DOI: 10.1021/acs.cgd.8b00546
Cryst. Growth Des. 2018, 18, 5099−5107

parallel to the [011] and [01−1] directions on the substrate.[8,29−31] In these studies, attention was mainly focused on the crystallographic match and minimization of the interfacial energy. In our paper, we investigate the epitaxial crystallization of anthraquinone on (100) NaCl surfaces from the vapor phase under well-controlled conditions (Figure 1).

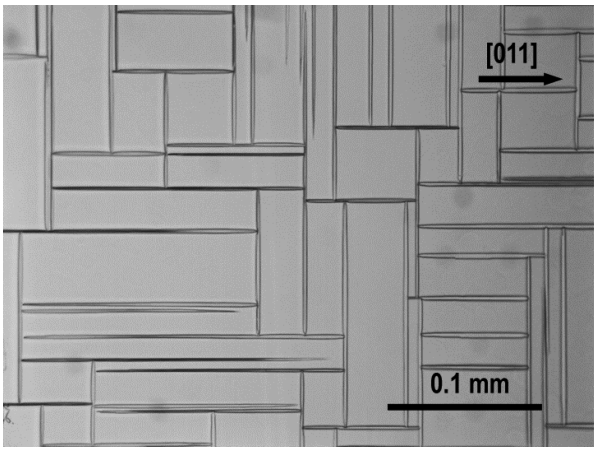


**Figure 1.** Scanning electron micrograph showing a Mondriaan-like pattern of oriented anthraquinone crystal needles grown from the vapor on top of a (100) NaCl substrate.

This is realized by direct observation of the nucleation and the subsequent growth process as a function of supersaturation using optical microscopy. The optical in situ observations are supplemented by atomic force microscopy (AFM), scanning electron microscopy (SEM), and X-ray diffraction. The results obtained are interpreted using different crystal growth models, involving, among others, 3D epitaxial nucleation and surface diffusion. In this way, insight is obtained in the epitaxial growth of organic crystals on foreign substrates.

## 2. EXPERIMENTAL SECTION

**2.1. Driving Force.** For crystal growth from the vapor, the dimensionless driving force, $\Delta\mu/kT$, is given by

$$\frac{\Delta\mu}{kT} = \ln\left(\frac{P}{P_{eq}}\right) \tag{1}$$

with $P$ and $P_{eq}$ the actual and the equilibrium vapor pressures, respectively. If vapor transport of material from the source at $T_{source}$ to the growing crystals at $T_{sub}$ is fast, growth is completely determined by surface kinetics. Using $P_{eq} \propto \exp(-\Delta H_{evp}/RT)$, one then obtains a driving force

$$\frac{\Delta\mu}{kT} = \frac{\Delta H_{evp}}{R}\frac{\Delta T}{T_{source}T_{sub}} \tag{2}$$

with $\Delta T = T_{source} - T_{sub}$.

The sublimation (evaporation) enthalpy $\Delta H_{evp}$ of anthraquinone is 26.7 kcal/mol in the temperature range of 300 to 360 K,[32] which is used in our experiments.

**2.2. Growth Cell.** A growth cell suitable for microscopic in situ observation of well-controlled crystal growth processes from the vapor is used. This growth cell, shown in Figure 2, has been detailed in ref 21. In brief, the sodium chloride substrate is placed on the central cylindrical stage in the cell. The temperature of the substrate, $T_{sub}$, is measured by a thermocouple clamped on its top face and is controlled by a Peltier heating/cooling element (±0.1 K). A large excess of anthraquinone source material is placed around the central substrate stage and is kept at $T_{source}$ within 0.1 K using a thermostated water

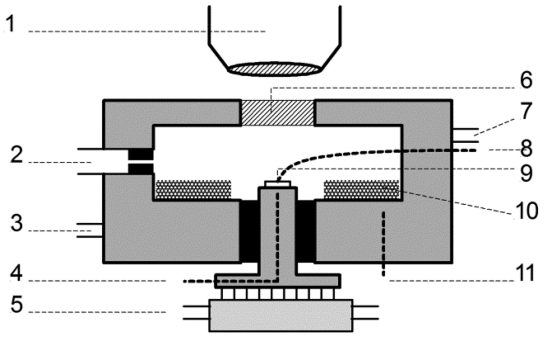


**Figure 2.** Vapor growth cell. (1) Microscope objective, (2) vacuum outlet plus diaphragm, (3) thermostated water inlet, (4) thermocouple for substrate temperature control, (5) Peltier element plus water cooling, (6) sapphire window, (7) thermostated water outlet, (8) thermocouple for substrate temperature, $T_{sub}$, measurement, (9) substrate, (10) source material, (11) thermocouple for $T_{source}$ measurement. Outer diameter growth cell, ~10 cm.

flow around the cell. The cell is connected to an oil diffusion pump, which keeps the total pressure in the cell below 0.01 Pa. In this way, the vapor pressure of the anthraquinone in the whole cell volume is determined by the equilibrium pressure at $T_{source}$ ($6.3 \times 10^{-4}$ Pa at 325 K), and for a given $T_{sub}$, $\Delta\mu/kT$ can now readily be calculated using eq 2. To ensure that pumping does not cause large amounts of source material to be removed from the cell, a diaphragm (⌀ = 1 mm) is placed between the pump and the cell. The growth cell is covered by a sapphire window, through which the growth of the crystals can be monitored using a reflection optical microscope (Nikon Microphot FX) equipped with a CCD camera. This allows measuring growth rates by analyzing a sequence of pictures of the growth process recorded at known time intervals.

**2.3. Experimental Procedure.** Experiments were performed using fixed source temperatures, $T_{source}$, between 313 and 333 K, and the supersaturation $\Delta\mu/kT$ was varied from 0.3 to 2.3 by control of $T_{sub}$.

The {100} substrate crystals were obtained from a large melt grown NaCl single crystal (Korth Kristalle GmbH), which was cleaved into pieces of 4 × 4 $mm^2$ and 2 mm thickness. Cleavage, sample preparation, and postgrowth examination were done in a room with relative humidity (RH) below 40%. Around and below this RH, the first monolayer of water on top of the {100} NaCl faces is "frozen," and no step mobility occurs.[33,34] Anthraquinone powder (97%, Aldrich) was used as a source material.

Prior to growth, the cleaved NaCl substrate was clamped onto the substrate holder in the cell by the thermocouple to ensure a good thermal contact. After placing an excess of anthraquinone powder around the central stage, the cell was closed and evacuated. The temperature of the cell and the substrate was raised to the desired value of $T_{source}$, keeping $T_{sub} > T_{source}$ to avoid preliminary crystallization on the substrate. Then, the substrate temperature was lowered within 2 min to obtain the appropriate—stable—substrate temperature, $T_{sub}$. The growth runs were stopped by venting the cell with air, which nearly completely blocks the transport of anthraquinone. This prevents a shut-off effect by which the substrate becomes covered by unwanted anthraquinone material.[35]

**2.4. Characterization Methods.** Aside from in situ recording using reflection optical microscopy during growth, the anthraquinone crystals were also examined after removal of the substrate from the cell. The ex-situ examinations were performed using optical polarization microscopy (Leica DM RX), scanning electron microscopy (SEM), and atomic force microscopy (AFM). SEM was performed to obtain quantitative information on the 3D morphology of the crystals. Prior to SEM, the specimens were sputter coated with a thin film of Pt−Pd. Analysis of the growth mechanisms of the different anthraquinone faces was performed using contact mode AFM. For this, a Digital Instruments Nanoscope III, equipped with


DOI: 10.1021/acs.cgd.8b00546
Cryst. Growth Des. 2018, 18, 5099−5107

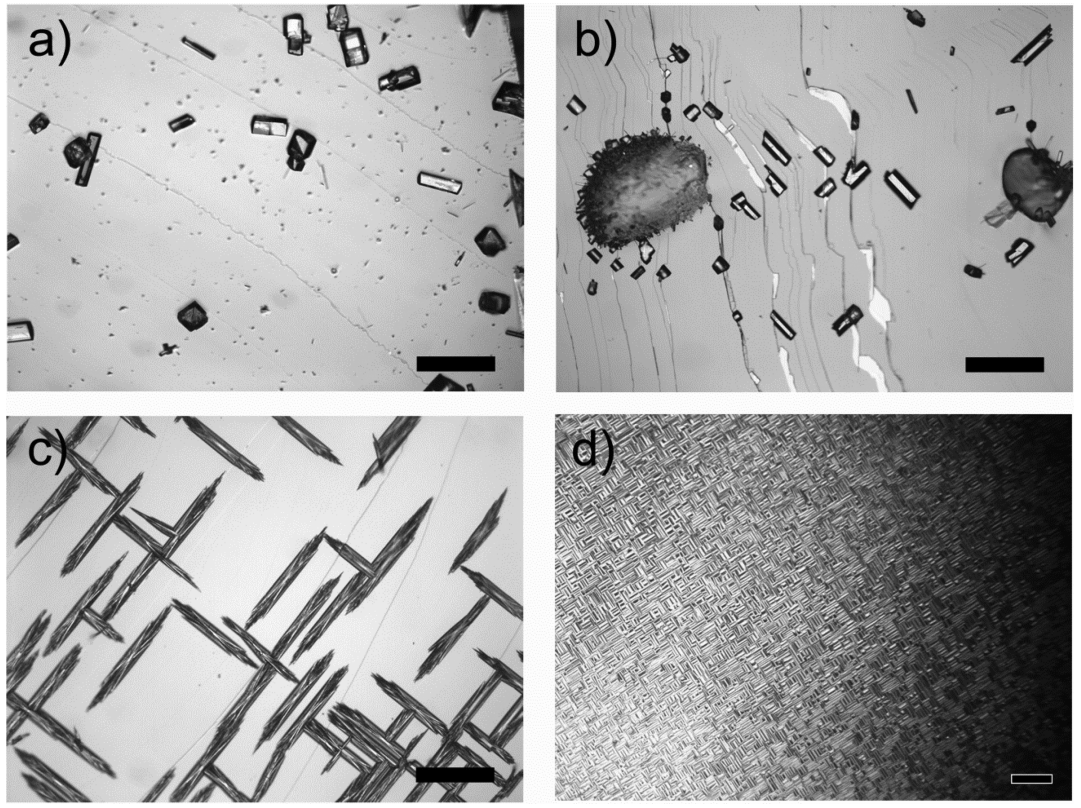


**Figure 3.** Anthraquinone on {100} NaCl. (a) $T_{source}$ = 322.4 K, $T_{sub}$ = 321.6 K, $\Delta\mu/kT$ = 0.1, scale bar = 0.2 mm; (b) $T_{source}$ = 312.5 K, $T_{sub}$ = 310.6 K, $\Delta\mu/kT$ = 0.26, scale bar = 0.1 mm; (c) $T_{source}$ = 322.4 K, $T_{sub}$ = 311.2 K, $\Delta\mu/kT$ = 1.5, scale bar = 0.1 mm; (d) $T_{source}$ = 322.5 K, $T_{sub}$ = 304.9 K, $\Delta\mu/kT$ = 2.4; scale bar = 0.02 mm.

silicon nitride cantilevers with spring constants ranging from 0.1 to 0.5 N/m, was used. X-ray diffraction was used to determine the relative orientation of the anthraquinone crystals on the (100) NaCl substrate.

## 3. RESULTS AND DISCUSSION

**3.1. Epitaxy and Morphology.** More than 200 experiments have been performed. A selection of results at different driving forces, recorded by optical microscopy, is shown in Figure 3a–d.

For $\Delta\mu/kT$ < 0.25, no epitaxial growth was found, and the grown anthraquinone crystals were randomly oriented on the substrate surface (Figure 3a). We think that, here, nucleation occurred at foreign particles on the surface, possibly some nano- or micrograins originating from NaCl cleavage or spilled from the source material. The density of the nuclei is low.

At driving forces $\Delta\mu/kT$ > 0.25 and vapor temperatures, $T_{source}$, between 313 and 333 K, epitaxial growth was observed, with slowly increasing crystallite densities for increasing $\Delta\mu/kT$. The majority of the needle crystals were oriented with their needle axis parallel to the two <011> directions on the (100) NaCl substrate (Figure 3b and c). A smaller group of needles (~10%) was oriented + or −11.5° with respect to the main group, which corresponds to the eight <023> directions on the substrate (Figure 4).

At driving forces beyond $\Delta\mu/kT \approx 1.9$, a sudden rise in needle density occurs. The surface is completely covered by a high density of small, epitaxial needles parallel to <011> on (100) NaCl (Figure 3d).

The morphology of the epitaxial anthraquinone crystals depends on the supersaturation as follows from Figure 3b–d.

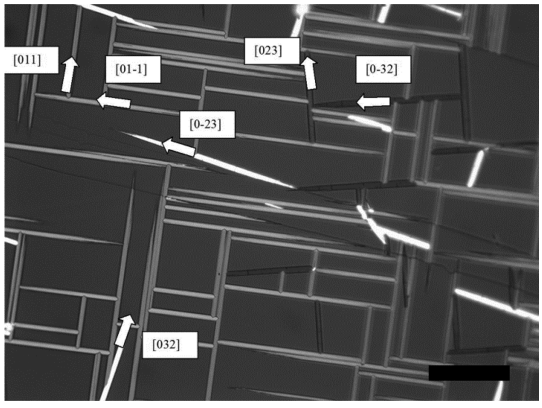


**Figure 4.** Optical polarization micrograph showing the different epitaxial orientations of anthraquinone on (100) NaCl. The main group of needles points toward the [011] and [0−11] directions of the substrate. $T_{source}$ = 334.7 K, $T_{sub}$ = 324.4 K, $\Delta\mu/kT$ = 1.27, scale bar = 0.1 mm.

At the lower driving forces 0.25 < $\Delta\mu/kT$ < 0.6, the needles are block shaped with flat end and side faces as schematized in Figure 5. The morphology and orientation of these crystals is determined using SEM and X-ray diffraction. Only the needles oriented along the <011> substrate directions are considered. The contact face of the monoclinic anthraquinone crystals (space group: $P2_1/c$, $a$ = 7.87, $b$ = 3.96, $c$ = 15.78 Å, and $\beta$ = 102.7°[36]) with the substrate is (10−2). This implies that the plane of the anthraquinone molecules, i.e., the line connecting the two oxygen atoms of each molecule, is oriented more or less perpendicular to the substrate surface, as shown in Figure



DOI: 10.1021/acs.cgd.8b00546
Cryst. Growth Des. 2018, 18, 5099−5107

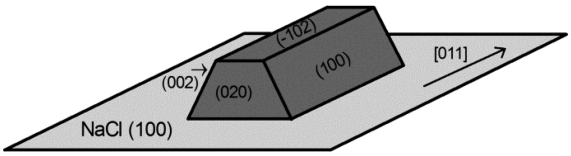


**Figure 5.** Morphology of anthraquinone on (100) NaCl.

6. This is different from the well studied larger (planar) molecule PTCDA. Here, thick films grown by MBE again show the same structure as the bulk phase, but now with the molecular plane parallel to the graphite substrate surface.[17] The lattice mismatch of the (1 0−2) anthraquinone face in contact with the (100) NaCl substrate is low. The anthraquinone $b$ axis (3.963 Å) and its perpendicular vector $2\vec{a} + \vec{c}$ (19.67 Å) correspond with the 1/2[011] (3.988 Å) and the 5/2[01−1] (19.94 Å) distances of the (100) NaCl surface, respectively (Figure 6b). In the notation introduced by Hooks et al.,[16] this is

$$\begin{matrix} \vec{b}_{AQ} \\ [201]_{AQ} \end{matrix} = \begin{bmatrix} 1/2 & 1/2 \\ 5/2 & -5/2 \end{bmatrix} \begin{matrix} \vec{b}_{NaCl} \\ \vec{c}_{NaCl} \end{matrix}$$

These values stand for a lattice mismatch of 0.62% and 1.4% in the two directions.

To accommodate this minor lattice mismatch, the lowest molecular anthraquinone layer(s) may be somewhat different from the layers above, being adapted by elastic deformation, dislocations,[37] slight rotation,[16,17] or static distortion waves.[20] So, the actual accommodation of the epitaxial crystals to the substrate, determined by the lowest molecular layers, is in fact a more complex issue, the secrets of which are hidden by the overgrown crystal.

The end faces of the block shaped needles are {020}, the side faces are (100) and (002), and the upper face is (−102) as depicted in Figure 5.

The needle orientation was confirmed by optical polarization microscopy. Extinction occurs if the crossed polarizers are parallel and perpendicular to the needle axis, which is parallel to the $b$ axis of the anthraquinone structure. This matches with the point group 2/m of the crystals, where the mirror plane is perpendicular to the needle axis.

Atomic force microscopy of the (−102) top faces shows that this face grows via steps of 0.7 and 1.4 nm in height (Figure 7a), which corresponds with half and one unit cell height in this direction ($d_{10-2}$ = 0.69 nm). The steps originate from growth spirals. The (100) and (002) side faces also show low steps, being 0.7 and 1.3 nm in height (Figure 7b). Here, steps originate from spirals as well as from the contact line between the substrate and crystal. No evidence of a posteriori evaporation of the crystals was found by AFM.

At higher supersaturation, $\Delta\mu/kT > 0.6$, the {020} end faces of the needle crystals are no longer flat but split up into many ultrathin needles (Figures 3c and 8). This points to kinetic roughening[38,39] of this face, which in turn leads to morphologic instability.[40,41] In the supersaturation range $1 < \Delta\mu/kT < 2$, the tips of the ultrathin needles are rounded with a radius between 0.11 and 0.14 $\mu$m, as was measured by SEM.

At the highest supersaturation $\Delta\mu/kT \geq 1.9$, a sudden, dramatic increase in epitaxial needle density occurs, as shown in Figure 3d. The morphology and orientation of the crystals is similar to that found in the $1 < \Delta\mu/kT < 2$ regime, including the thin needle splitting at the tips. The average needle length

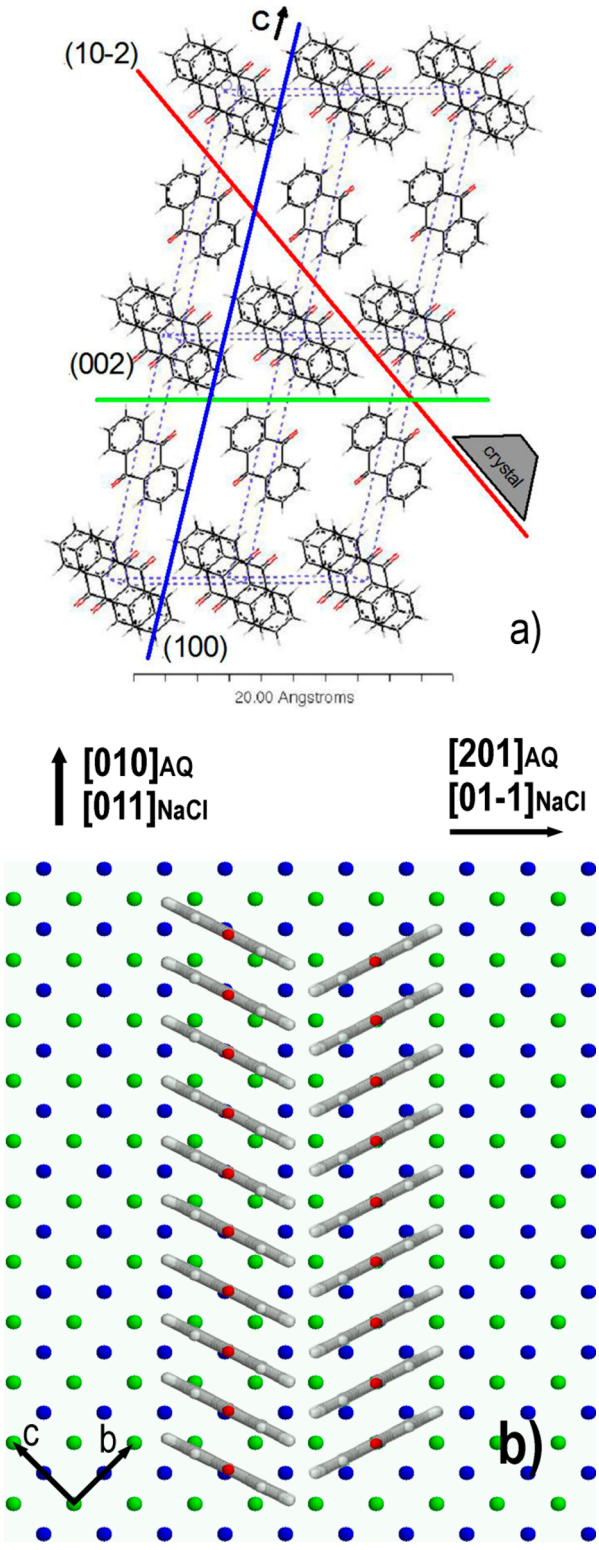


**Figure 6.** Anthraquinone on (100) NaCl: (a) red line, anthraquinone (10−2) contact face; green line, (002) side face; and blue line, (100) side face; view projected along ~[020]. (b) View from top including the (100) NaCl substrate surface, showing the near lattice match in two perpendicular directions. Blue, $Na^+$; green, $Cl^-$.

is small as the growing needles collide against their neighbors and stop growing.

**3.2. Nucleation.** As concerns the nucleation of the anthraquinone crystals on the (100) NaCl substrates, we can



DOI: 10.1021/acs.cgd.8b00546
Cryst. Growth Des. 2018, 18, 5099−5107

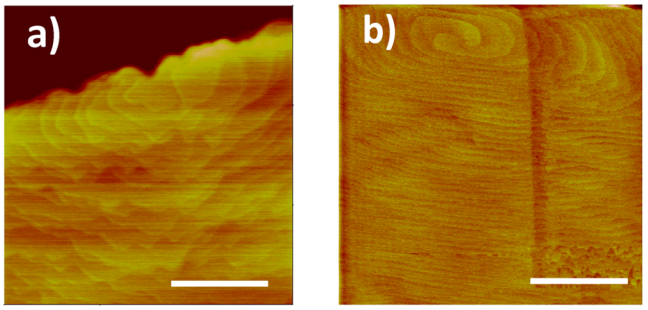


**Figure 7.** (a) AFM micrograph of the (−102) top face of anthraquinone ($T_{source}$ = 313.0 K, $T_{sub}$ = 306.8 K, $\Delta\mu/kT$ = 0.89). (b) AFM micrograph of the (100) or (002) side face of anthraquinone showing a double spiral pattern ($T_{source}$ = 314.0 K, $T_{sub}$ = 311.0 K, $\Delta\mu/kT$ = 0.52). Scale bar in both images = 1.0 $\mu$m.

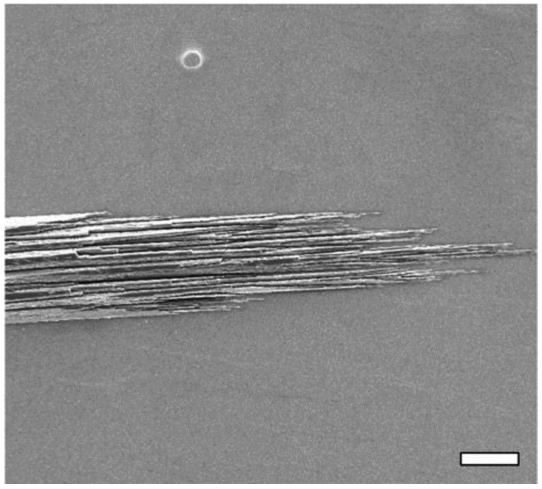

**Figure 8.** SEM micrograph showing tip splitting of the anthraquinone face (020) end face into numerous ultrathin needles ($T_{source}$ = 322.5 K, $T_{sub}$ = 308.1 K, $\Delta\mu/kT$ = 1.94, scale bar 10 $\mu$m).

distinguish three supersaturation regimes (Figures 3 and 9): (I) At $\Delta\mu/kT$ < 0.25, no epitaxial nucleation was encountered, and the density of the nuclei was very low. The randomly oriented, block shaped anthraquinone crystallites (Figure 3a) probably originate from dust, submicron anthraquinone

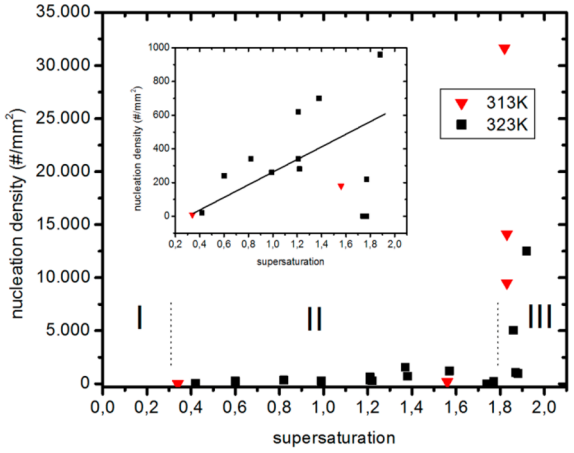


**Figure 9.** Nucleation density of the anthraquinone crystallites as a function of driving force $\Delta\mu/kT$, showing the three supersaturation regimes. $T_{source}$ is 313 or 323 K.

particles "spilled" from the source material, or very small NaCl particles that formed during NaCl cleavage. (II) For 0.25 < $\Delta\mu/kT$ < 1.9, epitaxial nucleation takes place at relatively low densities, generally starting from cleavage macrosteps on the NaCl substrate (Figure 3b and c). The cleavage process to obtain the (100) faces gives rise to a higher macrostep density at the peripheral regions of the substrate and thus to a higher nuclei density at these places. Sloat and Menzies already noted this.[10] All crystallites nucleated at approximately the same time, when the cell had reached stable conditions. After this period, the crystals grew further, but no additional nuclei were formed. First growing at a low driving force and then increasing the supersaturation by lowering the substrate temperature gives rise to additional nucleation between the crystals already formed. The increase in nuclei density as a function of driving force follows $N_{nucl} \approx 380 \times \Delta\mu/kT$ mm$^{-2}$ (Figure 9), but with a very large spread in the values. The preferential nucleation at macrostep sites is explained by a lower activation barrier as compared to nucleation on the planar (100) face. The relatively low number of nuclei formed is due to the limited number of macrosteps, i.e., a restricted number of nucleation sites. As the activation barrier for nucleation lowers for increasing driving force, also less favorable sites at the macrosteps become available; this increases the number of nuclei. (III) For $\Delta\mu/kT$ > 1.9, a sudden, dramatic increase in nucleation density of 1 to 2 orders of magnitude is observed everywhere on the substrate (Figures 3d and 9). Here, the epitaxial nucleation likely occurs on the ideally flat (100) surfaces or at the multitude of monatomic steps and not only at the macrosteps. Nucleation at the monatomic steps could not be verified by AFM as the relatively large crystallites mask the original sites of their birth. The nucleation does not take place at preferred positions on the substrate. This was verified by repeating growth at a driving force $\Delta\mu/kT$ = 2.0 and $T_{source}$ = 318 K followed by complete evaporation of the crystals by raising $T_{sub}$. After seven cycles of growth and etching, nucleation did not happen even once at the same place on the substrate. The crystals nucleate at random, although some preferential nucleation still occurs at the macrosteps. As a consequence of the higher driving force, the activation barrier for nucleation is so low that germs can easily be formed on the plane (100) substrate or at monatomic steps. As the number of suitable sites is now orders of magnitude larger than the sites at the macrosteps, the number of nuclei increases greatly, despite the activation barrier being higher.

**3.3. Growth.** To obtain evidence for surface diffusion on the substrate, growth rates of the anthraquinone crystals were measured as a function of $T_{source}$ and $T_{sub}$ (i.e., $\Delta\mu/kT$). Figure 10 shows the length increase of two different anthraquinone needles as a function of time. One crystal grew in two directions, the second one in one direction due to an early collision with another needle. It can be seen that the growth rate is constant in time. This constant speed was observed for all experiments, even on a time scale of days, demonstrating the stability of the growth setup. The growth rates were obtained from half the slope of the linear least-square fit of the growth curves of those crystals that grew in both directions.

Growth rates for the different $T_{source}$ values as a function of $\Delta\mu/kT$ are given in Figure 11, both for the longitudinal and lateral directions of the needles. It is clear that the growth rates increase for increasing $T_{source}$ and $\Delta\mu/kT$. Figure 12 shows the logarithm of the growth rate for $T_{source}$ = 318 K as a function of $\Delta\mu/kT$ for both the longitudinal and the lateral directions. A



DOI: 10.1021/acs.cgd.8b00546
Cryst. Growth Des. 2018, 18, 5099−5107

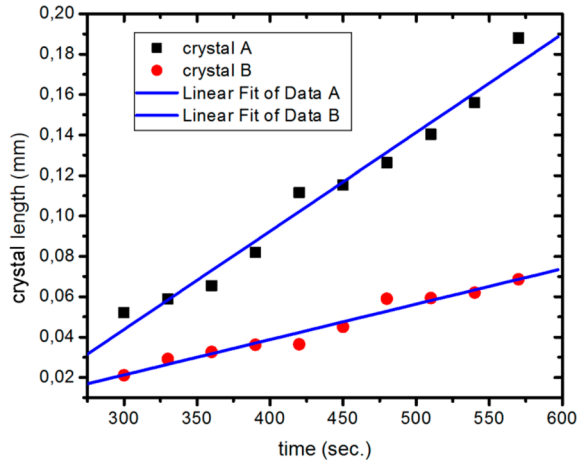


**Figure 10.** Longitudinal crystal length as a function of time from the start of the experiment for two different crystals A and B. Crystal A grows in two directions, crystal B only in one direction. $T_{source}$ = 333 K, $\Delta\mu/kT$ = 1.6.

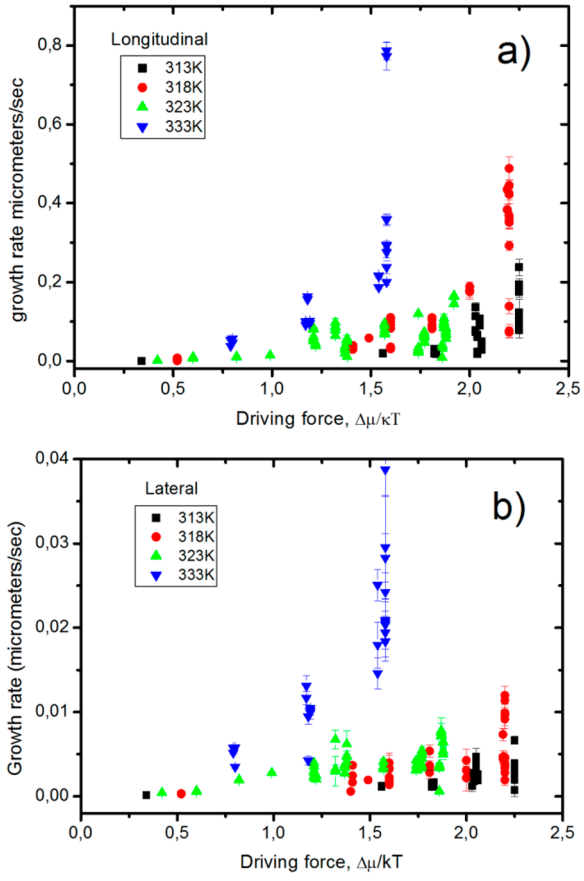


**Figure 11.** Longitudinal (a) and lateral (b) growth rates as a function of the driving force for the four $T_{source}$ values used in this study.

similar exponentional behavior (or power law in terms of pressure) of the growth rate

$$R = K\exp(A\cdot\Delta\mu/kT),\ \ln R = A\cdot\Delta\mu/kT + B \text{ or}$$

$$R = K\left(\frac{P}{P_{eq}}\right)^{A} \quad (3)$$

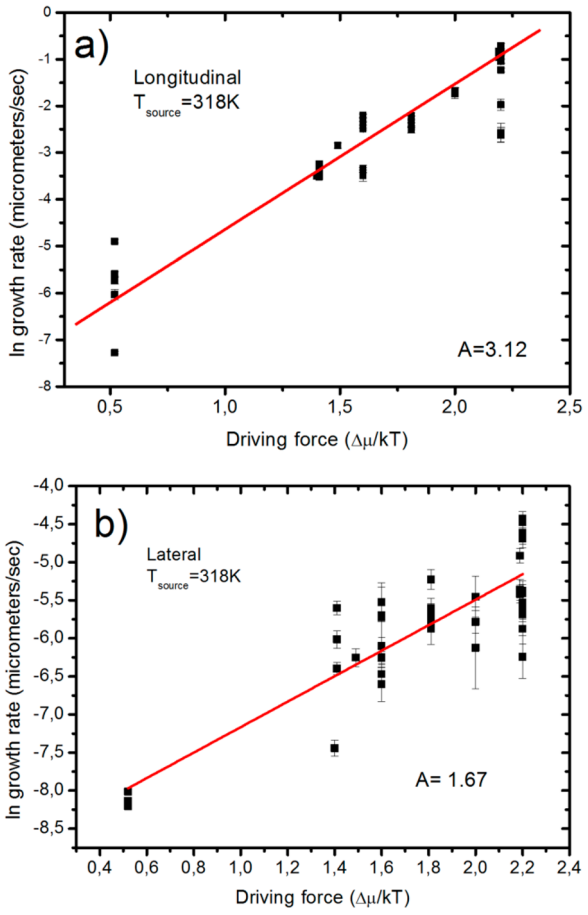


**Figure 12.** Logarithm of the anthraquinone crystal growth rates in the longitudinal (left) and the lateral (right) directions as a function of the driving force, $\Delta\mu/kT$, at $T_{source}$ = 318 K.

was also found for the other three $T_{source}$ values (313, 323, and 333 K) in the interval $\Delta\mu/kT$ = 0.4−2.5 (Supporting Information S1). Here, $A$ and $K$ are constants. For $T_{source}$ = 313 to 333, $A$ goes from 3.4 to 2.6 for length growth and is around 1.75 for width growth (Figure 13). This dissimilarity is likely due to the larger influence of crystal incorporation kinetics after surface diffusion for width growth as compared to length growth.

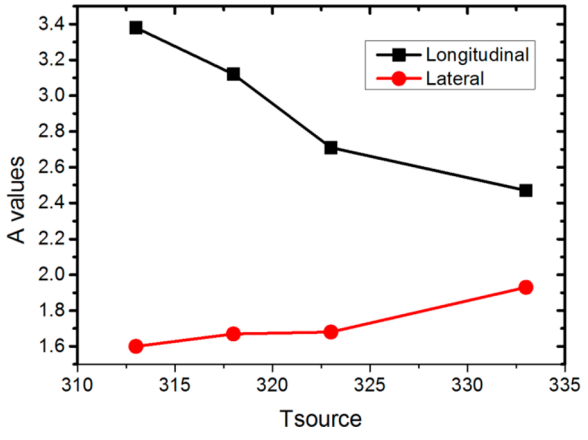


**Figure 13.** $A$ values (in eq 3) for longitudinal and lateral growth rates.



DOI: 10.1021/acs.cgd.8b00546
Cryst. Growth Des. 2018, 18, 5099−5107

**3.4. Surface Diffusion.** As elucidated in Supporting Information SI 2, the maximum needle growth rate, if growth is determined by the direct impingement of growth units on the top faces, is given by

$$v_{max}^{long} = V_{cell}\frac{P}{\sqrt{2\pi mkT}}S \quad (4)$$

Here, $v_{max}^{long}$ is the maximal growth rate in the needle's length direction; $P$, the anthraquinone vapor pressure at $T_{source}$; $m$, the mass of one anthraquinone molecule; and $S$, the sticking fraction. $V_{cell}$ is the volume of the crystallographic unit cell containing two anthraquinone molecules. The maximal value of $S$ is 1. The maximal growth rates calculated for the different $T_{source}$ values are summarized in Table 1.

**Table 1. Calculated Maximum Tip Growth Rates, Assuming No Surface Diffusion, for Different Vapor Source Temperatures**

| $T_{source}$ in K | maximal growth rate without surface diffusion ($\mu$m/s) |
|---|---|
| 313 | $6.43 \times 10^{-4}$ |
| 318 | $1.25 \times 10^{-3}$ |
| 323 | $2.38 \times 10^{-3}$ |
| 333 | $8.13 \times 10^{-3}$ |

It is clear that the maximal growth rates in Table 1 are far less than the observed values, which range between $3 \times 10^{-3}$ $\mu$m/s for the lowest $\Delta\mu/kT$ to 0.5 $\mu$m/s for the highest driving forces (Figure 11). This indicates that the dominant supply of growth units to the needle tips must proceed via diffusion over the (100) NaCl surface. Diffusion over the needle's upper and side faces toward the tip does not play a main role as the length growth rate of the crystals does not increase in time, but remains constant (Figure 10).

Figure 14 shows the route of the growth units toward the crystal surfaces. Tip growth proceeds via surface diffusion over

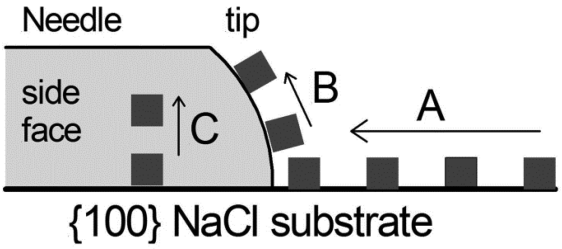


**Figure 14.** Route of the anthraquinone growth units toward the needle's tip and side faces.

the substrate (A) followed by surface diffusion over and subsequent incorporation into the tip surface (B). For higher supersaturations, $\Delta\mu/kT > 0.6$, the tips are pointed and show splitting, which indicates mass transport limited growth in step A, followed by rapid incorporation in step B. At lower supersaturation, the tip face is faceted, and growth rates are low. Here, the tip is not kinetically roughened, and step B partially slows down the growth rate. The latter also holds for the slower growth of the planar needle side faces, here, step C. From the above, it is clear that to permit crystal growth via supply of growth units over the substrate surface, surface diffusion on the anthraquinone crystal surfaces is also needed.

Additional evidence for this surface diffusion controlled growth is the occurrence of the splitting of the needle top faces at higher supersaturation (Figure 8), which is characteristic for morphologic instability. Morphological instability is common in transport limited growth,[40,41] which in our case is surface diffusion over the substrate surface. The decrease of needle tip radius with increasing supersaturation (compare Figure 3b to d) is also characteristic for mass transport limited growth.[42] Surface diffusion also explains that the needles nucleate at approximately the same moment. After nucleation, the crystals start to grow and deplete the substrate surface area around from growth units, which prohibits the formation of additional nuclei.

The diffusion length of the ad-molecules can be estimated from the decrease in growth rate if two crystals approach each other competing for surrounding ad-molecules. However, in our case, no decrease in growth rate was found, but in view of the resolution of the optical system used, it should be realized that no accurate growth rate change measurements could be performed for intercrystal distances less than 10−20 $\mu$m.

Molecular details of the adsorption and transport of the anthraquinone units on the substrate surface are not given here, as this requires molecular dynamics simulations, which is beyond the scope of this experimental paper. Computer modeling nevertheless can provide an estimate of the orientation and density of the adsorbed anthraquinone molecules. Supporting Information S3 gives a discussion on the surface coverage of the anthraquinone molecules on the (100) NaCl surface. The energetically most favorable orientation of a single adsorbed anthraquinone molecule is planar with its length direction pointing toward one of the <001> directions on the (100) NaCl surface (Figure 15).

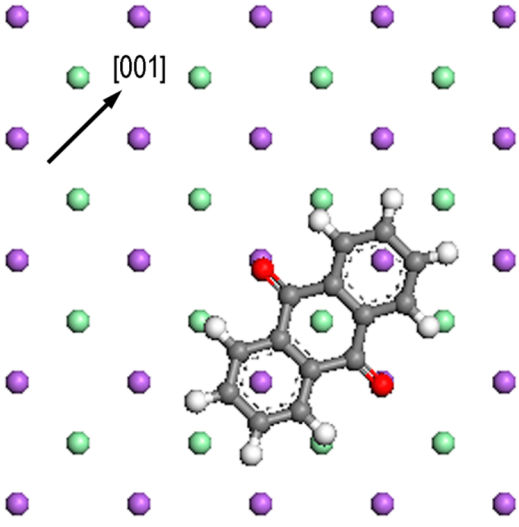


**Figure 15.** Minimum energy configuration of an isolated adsorbed anthraquinone molecule, laying flat and pointing its length direction toward [001] on the (100) NaCl substrate. Green, $Cl^-$; purple, $Na^+$.

Here, the negatively charged oxygen atoms of the anthraquinone molecule strongly interact with the $Na^+$ substrate ions. DFT calculation gives an adsorption energy of 0.54 eV/molecule. However, the DFT method used here underestimates the attractive van der Waals interaction to some extent, which has an essential contribution to the adsorption energy as shown by Aldahhak et al. for a similar but larger molecule on (001) NaCl.[43] So, the actual adsorption energy is likely 0.1−0.2 eV higher. As elaborated in S3, this corresponds to a surface coverage ranging from $\theta$ = 0.02 to 0.40, far from


DOI: 10.1021/acs.cgd.8b00546
Cryst. Growth Des. 2018, 18, 5099−5107

the needle crystals, which is sufficient for the surface diffusion controlled supply of growth units. Unfortunately, the surface diffusion coefficient of anthraquinone molecules on (100) NaCl is not known. In addition, it should be realized that the situation is further complicated by the possible presence of "frozen" water molecules on the NaCl surface.[33,34] Therefore, an advanced molecular modeling, including the occurrence of water, is needed to clarify the situation more precisely.

The planar orientation of an isolated diffusing molecule is determined by the substrate−molecule interaction. A 2D or 3D crystal nucleus is formed by tipping up the flat laying molecules, leading to a perpendicular orientation, contacting adjacent perpendicular molecules as drawn in Figure 6. Here, the intermolecular interactions play an essential role as well.

**3.5. Mechanisms of Growth.** Finally, it is to be realized that relation 3 is purely empirical as the growth process is complex and involves several coupled processes occurring simultaneously. In all cases, the supply of growth units proceeds by surface diffusion, but at the lowest supersaturation, interface kinetics plays a role as well, leading to faceted top faces. At higher supersaturation, kinetic roughening sets in, giving nonfaceted top faces, and at the highest supersaturation, growth is completely controlled by surface mass transport leading to morphological instability. In fact, the three supersaturation domains each follow a different $R(\Delta\mu/kT)$ behavior, but this is neglected in the very approximate eq 3. Detailed interpretation would be too speculative and therefore is avoided.

## 4. CONCLUSIONS

The vapor growth crystallization of anthraquinone on {100} NaCl substrates has been investigated quantitatively as a function of driving force, $\Delta\mu/kT = \ln(P/P_{eq})$. Morphology, nucleation rates, and growth rates have been studied. For this purpose, a growth cell has been designed that allows for in situ observation of the growth process at well-defined conditions using optical microscopy. Ex-situ characterization of the deposits was performed using SEM, AFM, and polarization microscopy.

Epitaxial growth of anthraquinone crystals sets in from driving forces $\Delta\mu/kT > 0.3$. The majority of the needle shaped crystals grow in the <011> directions of the substrate and a minority (∼10%) in the <023> directions. The anthraquinone contact face with the substrate is (10−2). Further, the morphology of the needle crystals is bounded by (100) and (002) side faces, a (−102) upper face, and {020} tip faces. For $\Delta\mu/kT > 0.6$, the tip face is no longer faceted, but kinetically roughened.

The density of nuclei formed increases slowly from $\Delta\mu/kT$ = 0.3 to 1.8. Here, the epitaxial crystallites nucleate at the cleavage macrosteps on the NaCl substrates. From $\Delta\mu/kT$ = 1.9 and upward, the number density of nuclei rapidly increases by orders of magnitude. Here, nucleation occurs at random positions or at step sites of monomolecular height on the substrate.

The length and width growth rate of the epitaxial anthraquinone needles increases exponentially with $\Delta\mu/kT$. Comparing maximal tip growth rates calculated using kinetic gas theory with observed values shows that direct supply of growth units from the vapor phase to the crystal top surface is by far insufficient to explain the needle growth rates. Therefore, the main supply of growth units to the crystals proceeds via impingement on and subsequent diffusion over the NaCl substrate surface.

## ■ ASSOCIATED CONTENT

### Supporting Information

The Supporting Information is available free of charge on the ACS Publications website at DOI: 10.1021/acs.cgd.8b00546.

Logarithms of longitudinal and lateral crystal growth rates as a function of $\Delta\mu/kT$ for different $T_{source}$, maximal needle growth rates in absence of surface diffusion, and estimation of surface coverage of anthraquinone on (100) NaCl (PDF)

## ■ AUTHOR INFORMATION


### Corresponding Author

*Phone: 031-(0)24-3653433. E-mail: W.vanEnckevort@science.ru.nl.

### ORCID

Willem. J. P. van Enckevort: 0000-0001-7436-8391

Elias Vlieg: 0000-0002-1343-4102

### Present Addresses

§FOM Institute AMOLF, 1098 XG Amsterdam, The Netherlands

‖Abbott Healthcare Products BV, Manufacturing Science and Technology, Established Pharmaceuticals Division, C.J. van Houtenlaan 36, 1381 CP Weesp, The Netherlands


### Notes

The authors declare no competing financial interest.

## ■ REFERENCES


(1) Greene, J. E. Low-Energy Ion/Surface Interactions During Crystal Growth from the Vapor Phase: Effects on Nucleation and Growth, Defect Creation and Annihilation, Microstructure Evolution, and Synthesis of Metastable Phases. In *Handbook of Crystal Growth*; Hurle, D. T. J., Ed.; Elsevier: Amsterdam, 1993; Vol. *1a*, pp 639−681.

(2) Gilmer, G. H. Atomic-scale Models of Crystal Growth. In *Handbook of Crystal Growth*; Hurle, D. T. J., Ed.; Elsevier: Amsterdam, 1993; Vol *1a*, pp 583−637.

(3) Venables, J. A.; Spiller, G. D. T.; Hanbücken, M. *Rep. Prog. Phys.* **1984**, *47*, 399−459.

(4) See, for instance: Depuis, R. D. *J. Cryst. Growth* **1981**, *55*, 213−222.

(5) Amano, H.; Sawaki, N.; Akasaki, I.; Toyoda, Y. *Appl. Phys. Lett.* **1986**, *48*, 353−355.

(6) Nakamura, S. *Jpn. J. Appl. Phys. Part 2* **1991**, *30*, L1705−L1707. Nakamura, S.; Mukai, T.; Senoh, M. *Jpn. J. Appl. Phys. Part 2* **1991**, *30*, L1998−L2001.

(7) de Theije, F. K.; Zauner, A. R. A.; Hageman, P. R.; van Enckevort, W. J. P.; Larsen, P. K. *J. Cryst. Growth* **1999**, *197*, 37−47.

(8) Neuhaus, A. Z. *Phys. Chem.* **1943**, *192*, 309−331.

(9) Willems, J. *Naturwissenschaften* **1944**, *32*, 324−326.

(10) Sloat, C. A.; Menzies, W. C. *J. Phys. Chem.* **1930**, *35*, 2005−2021.

(11) Haber, T.; Resel, R.; Andreev, A.; Oehzelt, M.; Smilgies, D.-M.; Sitter, H. *J. Cryst. Growth* **2010**, *312*, 333−339.

(12) Schwabegger, G.; Djuric, T.; Sitter, H.; Resel, R.; Simbrunner, C. *Cryst. Growth Des.* **2013**, *13*, 536−542.

(13) Simmbrunner, C.; Sitter, H. Organic van der Waals Epitaxy versus Templated Growth by Organic-Organic Heteroepitaxy. In *Handbook of Crystal Growth: Thin Films and Epitaxy*, 2nd ed.; Keuch, T., Ed.; Elsevier: Amsterdam, 2015; Vol. *III*, part A, pp 483−508.

(14) Evans, P. G.; Spalenka, J. W. Epitaxy of Small Organic Molecules. In *Handbook of Crystal Growth: Thin films and epitaxy*, 2nd




DOI: 10.1021/acs.cgd.8b00546
*Cryst. Growth Des.* 2018, 18, 5099−5107

ed.; Keuch, T., Ed.; Elsevier: Amsterdam, 2015; Vol. *III*, part A, pp 509−554.
(15) See, for instance: Love, J. C.; Estroff, L. A.; Kriebel, J. K.; Nuzzo, R. G.; Whitesides, G. M. *Chem. Rev.* **2005**, *105*, 1103−1169.
(16) Hooks, D. E.; Fritz, T.; Ward, M. D. *Adv. Mater. (Weinheim, Ger.)* **2001**, *13*, 227−241.
(17) Ludwig, C.; Gompf, B.; Glatz, W.; Petersen, J.; Eisenmenger, W.; Möbes, M.; Zimmermann, U.; Karl, N. *Z. Phys. B: Condens. Matter* **1992**, *86*, 397−404.
(18) Schmidt, A.; Schuerlein, T. J.; Collins, G. E.; Armstrong, N. R. *J. Phys. Chem.* **1995**, *99*, 11770−11779.
(19) Ludwig, C.; Gompf, B.; Petersen, J.; Strohmaier, R.; Eisenmenger, W. *Z. Phys. B: Condens. Matter* **1994**, *93*, 365−373.
(20) Meissner, M.; Sojka, F.; Matthes, L.; Bechstedt, F.; Feng, X.; Müllen, K.; Mannsfeld, S. C. B.; Forker, R.; Fritz, T. *ACS Nano* **2016**, *10*, 6474−6483.
(21) Graswinckel, W. S.; van den Bruele, F. J.; van Enckevort, W. J. P.; Vlieg, E. *Cryst. Growth Des.* **2007**, *7*, 243−249.
(22) Leunissen, M. E.; Graswinckel, W. S.; van Enckevort, W. J. P.; Vlieg, E. *Cryst. Growth Des.* **2004**, *4*, 361−367.
(23) Mitchell, C. A.; Yu, L.; Ward, M. D. *J. Am. Chem. Soc.* **2001**, *123*, 10830−10839.
(24) Olmsted, B. K.; Ward, M. D. *CrystEngComm* **2011**, *13*, 1070−1073.
(25) Matsushige, K.; Hamano, T.; Horiuchi, T. *J. Cryst. Growth* **1995**, *146*, 641−644.
(26) Campione, M.; Sassella, A.; Moret, M.; Papagni, A.; Trabattoni, S.; Resel, R.; Lengyel, O.; Marcon, V.; Raos, G. *J. Am. Chem. Soc.* **2006**, *128*, 13378−13387.
(27) Sarma, K. R.; Shlichta, P. J.; Wilcox, W. R.; Lefever, R. A. *J. Cryst. Growth* **1997**, *174*, 487−494.
(28) van den Bruele, F. J.; Elemans, J. A. A. W.; Rowan, A. E.; van Enckevort, W. J. P.; Vlieg, E. *Langmuir* **2010**, *26*, 498−503.
(29) Kobzareva, S. A.; Distler, G. I. *J. Cryst. Growth* **1971**, *10*, 269−275.
(30) Willems, J. *Discuss. Faraday Soc.* **1958**, *25*, 111−113.
(31) Darling, D. F.; Field, B. O. *Surf. Sci.* **1973**, *36*, 630−640.
(32) Shimizu, T.; Ohkubo, S.; Kimura, M.; Tabata, I.; Hori, T. *J. Soc. Dyers Colour.* **1987**, *103*, 132−137.
(33) Foster, M. C.; Ewing, G. E. *J. Chem. Phys.* **2000**, *112*, 6817−6826.
(34) Arsić, J.; Kaminski, D. M.; Radenovic, N.; Poodt, P.; Graswinckel, W. S.; Cuppen, H. M.; Vlieg, E. *J. Chem. Phys.* **2004**, *120*, 9720−9724.
(35) van den Bruele, F. J.; Marks, K. M.; Harmsen, B.; Alfring, A. L.; Sprong, H.; van Enckevort, W. J. P.; Vlieg, E. *Cryst. Growth Des.* **2012**, *12*, 2265−2271.
(36) Fu, Y.; Brock, C. P. *Acta Crystallogr., Sect. B: Struct. Sci.* **1998**, *54*, 308−315.
(37) Frank, F. C.; van der Merwe, J. H. *Proc. R. Soc. London, Ser. A* **1949**, *198*, 216−225.
(38) Bennema, P. Growth and Morphology of Crystals. In *Handbook of Crystal Growth*; Hurle, D. T. J., Ed.; Elsevier: Amsterdam, 1993; Vol *1a*, pp 477−581.
(39) van Veenendaal, E.; van Hoof, P. J. C. M.; van Suchtelen, J.; van Enckevort, W. J. P.; Bennema, P. *Surf. Sci.* **1998**, *417*, 121−138.
(40) Billia, B.; Trivedi, R. Pattern Formation in Crystal Growth. In *Handbook of Crystal Growth*; Hurle, D. T. J., Ed.; Elsevier: Amsterdam, 1993; Vol *1b*, pp 899−1073.
(41) Coriell, S. R.; McFadden, G. B. Morphological Stability. In *Handbook of Crystal Growth*; Hurle, D. T. J., Ed.; Elsevier: Amsterdam, 1993; Vol *1b*, pp 785−857.
(42) Glicksman, M. E.; Marsh, S. P. The Dendrite. In *Handbook of Crystal Growth*; Hurle, D. T. J., Ed.; Elsevier: Amsterdam, 1993; Vol *1b*, pp 1075−1122.
(43) Aldahhak, H.; Schmidt, W. G.; Rauls, E. *Surf. Sci.* **2013**, *617*, 242−248.



DOI: 10.1021/acs.cgd.8b00546
*Cryst. Growth Des.* 2018, 18, 5099−5107